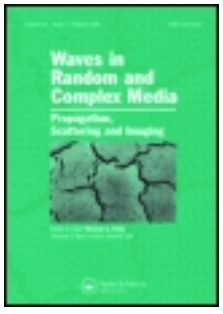

Waves in Random and Complex Media
Publication details, including instructions for authors and subscription information:
http://www.tandfonline.com/loi/twrm20

Double Dirac cones at k = 0 in pinned platonic crystals

Michael J.A. Smith[a], Ross C. McPhedran[b] & Michael H. Meylan[c]

[a] Department of Mathematics, The University of Auckland, Auckland, New Zealand.

[b] CUDOS ARC Centre of Excellence, School of Physics, University of Sydney, Sydney, Australia.

[c] School of Mathematical and Physical Sciences, The University of Newcastle, Newcastle, Australia.

Published online: 19 Dec 2013.

To cite this article: Michael J.A. Smith, Ross C. McPhedran & Michael H. Meylan , Waves in Random and Complex Media (2013): Double Dirac cones at k = 0 in pinned platonic crystals, Waves in Random and Complex Media, DOI: 10.1080/17455030.2013.862351

To link to this article: http://dx.doi.org/10.1080/17455030.2013.862351

Waves in Random and Complex Media, 2013
http://dx.doi.org/10.1080/17455030.2013.862351

Taylor & Francis
Taylor & Francis Group

Double Dirac cones at $\kappa = 0$ in pinned platonic crystals

Michael J.A. Smith[a*], Ross C. McPhedran[b] and Michael H. Meylan[c]

[a] *Department of Mathematics, The University of Auckland, Auckland, New Zealand;* [b] *CUDOS ARC Centre of Excellence, School of Physics, University of Sydney, Sydney, Australia;* [c] *School of Mathematical and Physical Sciences, The University of Newcastle, Newcastle, Australia*

(*Received 26 August 2013; accepted 26 October 2013*)

In this paper, we compute the band structure for a pinned elastic plate which is constrained at the points of a hexagonal lattice. Existing work on platonic crystals has been restricted to square and rectangular array geometries, and an examination of other Bravais lattice geometries for platonic crystals has yet to be made. Such hexagonal arrays have been shown to support Dirac cone dispersion at the center of the Brillouin zone for phononic crystals, and we demonstrate the existence of double Dirac cones for the first time in platonic crystals here. In the vicinity of these Dirac points, there are several complex dispersion phenomena, including a multiple interference phenomenon between families of waves which correspond to free space transport and those which interact with the pins. An examination of the reflectance and transmittance for large finite gratings arranged in a hexagonal fashion is also made, where these effects can be visualized using plane waves. This is achieved via a recurrence relation approach for the reflection and transmission matrices, which is computationally stable compared to transfer matrix approaches.

1. Introduction

In recent years, there has been significant research attention directed towards the dynamics of flexural wave energy through structured thin elastic plates. Such two-dimensional structures, known as platonic crystals, can be formed by periodically repeating any regular arrangement of scatterers embedded in a thin plate through to infinity. The simplest of these platonic crystals are those constructed using zero radius circular inclusions, or pins. Previous work in pinned elastic plates has been restricted to simple geometries such as square and rectangular lattices,[1–3] platonic clusters of square design,[1,4,5] and square stacks of gratings.[6] Attention has been paid towards stacks of shifted gratings,[7–9] however the investigations to date have been restricted to only two and three layers in depth.

These pinned platonic structures have been shown to exhibit several interesting and complex diffraction phenomena ranging from negative refraction in finite clusters [1] through to strong energy localization in defective platonic crystals.[10,11] Here, we consider a previously unexplored Bravais lattice geometry for the pin placement, and investigate an uninterrupted hexagonal lattice of pins. Accordingly, we are able to demonstrate the

*Corresponding author. Email: m.smith@math.auckland.ac.nz

existence of Dirac points and double Dirac cones for platonic crystals governed by the biharmonic plate equation.

Hexagonal arrays are of considerable interest at present due to ongoing research into the electronic properties of graphene, which is constructed as a hexagonal array of carbon atoms.[12] There is an established connection between hexagonal lattice geometries and degenerate band surfaces which give rise to Dirac points (DPs) and Dirac cones, a connection which is independent of the governing equation.[13] These DPs are defined as singularities in the band structure of a crystal where the spectral bands above and below the DP collapse as cones. That is, the band surfaces are degenerate and converge in the shape of cones to a single point in reciprocal space. In the center of this conical intersection, there is often a flat band which is associated with zero refractive index for photonic crystals,[13,14] zero permittivity and zero permeability ($\epsilon = \mu = 0$) in metamaterials,[15] zero mass density and infinite elastic moduli values in phononic crystals,[16] and zero effective mass for electrons.[12]

The use of the terms *Dirac points* and *Dirac cones* to describe this degeneracy arises from the problem of electron propagation through a hexagonal periodic potential (governed by the Schrodinger equation). The interaction of the electron with the lattice gives rise to quasiparticles that are governed by a relativistic form of the wave equation known as the *Dirac equation*.[12] It is indeed possible to engineer structures which exhibit Dirac cone dispersion by altering the properties of the scatterer (i.e. the radius) and in such cases DPs are said to arise from *accidental degeneracy*.[16–18] That said, in two-dimensional lattices, it is not unusual that bands are degenerate at symmetry points, such as the center or edge of the Brillouin zone.[19] There are previous instances of such behavior for a square pinned platonic crystal (of period unity) where the first, second, and third bands touch at the edge of the irreducible Brillouin zone.[3,4] Also, the existence of *Dirac–like* cones has been discussed in [20], arising from a platonic crystal design of clamped circular inclusions in a square array, and recently, the existence of double Dirac cones at the center of the Brillouin zone ($\boldsymbol{\kappa} = \mathbf{0}$) has been demonstrated by [15] for metamaterials. Additionally, it has been shown that a honeycomb lattice of masses and springs attached to a thin plate supports Dirac cone dispersion at the edge of the Brillouin zone.[21]

To the best of the authors' knowledge, this paper is the first investigation into hexagonally structured pinned plates in the literature, as well as the first paper to demonstrate the existence of double Dirac cones in platonic crystals. It is also the first time that Dirac cones have been investigated for a fourth-order system. It is important to emphasize that the free-space Green's function for the biharmonic plate equation is non-singular at the source. This feature of the Green's function, along with the higher order nature of the problem, makes it highly non-trivial that properties of Dirac cones for the Helmholtz equation carry over to the biharmonic plate equation. For photonic crystals, Dirac cones are associated with several interesting diffraction effects from pseudodiffusive transport [22] to conical diffraction.[13] For platonic crystals, we demonstrate here that resonances in transmission exist in the vicinity of double Dirac points. These resonances arise due to an overlapping of band surfaces, causing a Fabry–Perot style interference effect.

It is important to note that the dispersion relation for a pinned plate is singular at certain locations in reciprocal space. These singularities form surfaces throughout the Brillouin zone that are commonly referred to as *light lines* or *singularity surfaces*. Such surfaces provide upper and lower bounds for the band surfaces of pinned arrays, which may often be sandwiched between light lines.[4] In fact, for a square array of pins, there is band

sandwiching completely along the diagonals of the irreducible Brillouin zone.[4] Physically, these light lines correspond to frequencies and incident angles where plane wave propagation in free space is supported, i.e. in the absence of the platonic crystal.[2,4] An understanding of the intricate sandwiching of band surfaces between light lines is essential to clarify the intricate band structures we encounter here. It is also strongly connected with discussions of cloaking, which is described as *dynamic neutrality* in [4].

The outline of this paper is as follows. In Section 2, we provide an outline of the problem of wave scattering by an array of pins. This is followed by Section 3 where we compute the dispersion relation for a pinned plate. In Section 4, we demonstrate how to construct the reflection and transmission matrices of a single grating, and in Section 5, we consider the recurrence relation approach for computing the reflection and transmission matrices of a finite stack of N hexagonally arranged gratings. As a check on numerics, we provide the matrix form of the energy balance relation (for platonic crystals) in Section 6, before proceeding onto results in Section 7 and concluding remarks in the final section.

2. Problem formulation

We begin with the spectral representation of the Kirchoff–Love plate equation:

$$(\Delta^2 - k^4)w(\mathbf{x}) = (\Delta + k^2)(\Delta - k^2)w(\mathbf{x}) = 0, \tag{1}$$

where w is the plate displacement, $k^2 = \omega\sqrt{\rho h/D}$ is the non-dimensionalised wave number, ω is the angular frequency, ρ is the mass density, h is the thickness, D is the flexural rigidity of the plate, and $\mathbf{x} = (x, y)$. Additionally, we have assumed a time dependence of $\mathrm{e}^{-\mathrm{i}\omega t}$.

We are interested here with the dynamics of plates which are pinned in a doubly periodic fashion:

$$w(\mathbf{R}_p) = 0, \tag{2}$$

in accordance with the array vector

$$\mathbf{R}_p = m\begin{pmatrix} d \\ 0 \end{pmatrix} + n\begin{pmatrix} \xi \\ \eta \end{pmatrix}, \tag{3}$$

for $p = (m, n) \in \mathbb{Z}_2$ where d denotes the horizontal period, η the vertical period, and ξ the horizontal shift of each grating. For example, a square lattice of period d would have the parameter values $\xi = 0$ and $\eta = d$, whereas for a hexagonal lattice, we specify $\xi = d/2$ and $\eta = \sqrt{3}d/2$.

We begin by computing the dispersion relation for an arbitrary doubly periodic array of pins which are located at the coordinates given by the lattice vector $\mathbf{R}_p$, following the procedure outlined in [1].

3. Dispersion relation for a two-dimensional array of pins

In the absence of an incident wave, the displacement can be expressed in the form

$$w(\mathbf{x}) = \sum_{m=-\infty}^{\infty}\sum_{n=-\infty}^{\infty} a_{mn}\, g(|\mathbf{x} - \mathbf{R}_p|), \tag{4}$$

where $g(r)$ denotes the free-space Green's function for the biharmonic plate equation (1). This is given in closed form by

$$g(r) = \frac{\mathrm{i}}{8k^2}\left[H_0^{(1)}(kr) - \frac{2}{\pi \mathrm{i}} K_0(kr)\right], \tag{5}$$

where $r = |\mathbf{x} - \mathbf{x}'|$, $H_0^{(1)}$ is a zero-order Hankel function of the first kind and K_0 is a modified Bessel function of order zero.[23,24] Note that the Green's function for the plate is regular at $r \equiv 0$, in contrast to the Green's function for the Helmholtz equation. Here, we represent the location of the field point by $\mathbf{x}$ and the location of the source point by $\mathbf{x}'$.

One can then impose the quasi periodicity condition

$$w(\mathbf{x} + \mathbf{R}_p) = w(\mathbf{x})\mathrm{e}^{\mathrm{i}\boldsymbol{\kappa}\cdot\mathbf{R}_p}, \tag{6}$$

where $\boldsymbol{\kappa} = (\kappa_x, \kappa_y)$ denotes an arbitrary Bloch vector, to express (4) in the form

$$w(\mathbf{x}) = a_{00} \sum_{m=-\infty}^{\infty} \sum_{n=-\infty}^{\infty} \mathrm{e}^{\mathrm{i}\boldsymbol{\kappa}\cdot\mathbf{R}_p}\, g(|\mathbf{x} - \mathbf{R}_p|). \tag{7}$$

It is then possible to apply the boundary condition (2) at some arbitrary point $\mathbf{R}_{p'} = (\varrho, \varsigma)$ inside the Wigner–Seitz cell to obtain

$$\sum_p \mathrm{e}^{\mathrm{i}\boldsymbol{\kappa}\cdot\mathbf{R}_p}\, g(|\mathbf{R}_{p'} - \mathbf{R}_p|) = 0, \tag{8}$$

and use Graf's addition theorem

$$C_\nu(w)\mathrm{e}^{\mathrm{i}\nu\chi} = \sum_{l=-\infty}^{\infty} C_{l+\nu}(u) J_l(v)\mathrm{e}^{\mathrm{i}l\alpha}, \quad \text{where } |v\mathrm{e}^{\mathrm{i}\alpha}| < |u|, \tag{9}$$

(formula (9.1.79) in [25]) which is valid for any general Bessel function C_ν (i.e. J_ν, Y_ν, I_ν or K_ν) where the lines u, v, and w form a closed triangle with $w = \sqrt{u^2 + v^2 - 2uv\cos\alpha}$, where α denotes the angle between the lines u and v, and χ denotes the angle between the lines u and w. This allows us to write the component Bessel functions of (8) in the form

$$H_0^{(1)}(k|\mathbf{R}_{p'} - \mathbf{R}_p|) = \sum_{l=-\infty}^{\infty} H_l^{(1)}(k|\mathbf{R}_p|) J_l(k|\mathbf{R}_{p'}|)\mathrm{e}^{\mathrm{i}l(\arg\mathbf{R}_p - \arg\mathbf{R}_{p'})}, \tag{10a}$$

$$K_0(k|\mathbf{R}_{p'} - \mathbf{R}_p|) = \sum_{l=-\infty}^{\infty} K_l(k|\mathbf{R}_p|) J_l(k|\mathbf{R}_{p'}|)\mathrm{e}^{\mathrm{i}l(\arg\mathbf{R}_p - \arg\mathbf{R}_{p'})}, \tag{10b}$$

to obtain

$$\left[H_0^{(1)}(k|\mathbf{R}_{p'}|) - \frac{2}{\pi \mathrm{i}} K_0(k|\mathbf{R}_{p'}|)\right] + \sum_{l=-\infty}^{\infty} \left\{S_l^{\mathrm{H,A}}(k, \boldsymbol{\kappa}) - \frac{2}{\pi \mathrm{i}} S_l^{\mathrm{K,A}}(k, \boldsymbol{\kappa})\right\} J_l(k|\mathbf{R}_{p'}|)\mathrm{e}^{-\mathrm{i}l\arg\mathbf{R}_{p'}} = 0, \tag{11}$$

where

$$S_l^{\mathrm{H,A}}(k,\boldsymbol{\kappa}) = -\delta_{l,0} + \mathrm{i}S_l^{\mathrm{Y,A}}(k,\boldsymbol{\kappa}), \tag{12a}$$

$$S_l^{\mathrm{Y,A}}(k,\boldsymbol{\kappa}) = \sum_{p\neq(0,0)} Y_l(k|\mathbf{R}_p|)\mathrm{e}^{\mathrm{i}l\arg\mathbf{R}_p}\mathrm{e}^{\mathrm{i}\boldsymbol{\kappa}\cdot\mathbf{R}_p}, \tag{12b}$$

$$S_l^{\mathrm{K,A}}(k,\boldsymbol{\kappa}) = \sum_{p\neq(0,0)} K_l(k|\mathbf{R}_p|)\mathrm{e}^{\mathrm{i}l\arg\mathbf{R}_p}\mathrm{e}^{\mathrm{i}\boldsymbol{\kappa}\cdot\mathbf{R}_p}, \tag{12c}$$

[2,26]. If we then specify $\varrho = \varsigma = 0$ (i.e. impose the zero displacement condition at the origin), the expression (11) reduces to the well-known dispersion relation for a doubly periodic pinned plate:

$$S_0^{\mathrm{Y,A}}(k,\boldsymbol{\kappa}) + \frac{2}{\pi}S_0^{\mathrm{K,A}}(k,\boldsymbol{\kappa}) = 0, \tag{13}$$

[2,4]. Convergent expressions for the array sums (12b) and (12c) are provided in [2,27] where the zeroth-order terms are given by:

$$S_0^{\mathrm{Y,A}}(k,\boldsymbol{\kappa}) = -\frac{1}{J_3(k|\boldsymbol{\zeta}|)}\left(Y_3(k|\boldsymbol{\zeta}|) + \frac{1}{\pi}\sum_{n=1}^{3}\frac{(3-n)!}{(n-1)!}\left(\frac{2}{k|\boldsymbol{\zeta}|}\right)^{5-2n} + \frac{4}{A}\sum_p\left(\frac{k}{|\mathbf{Q}_p|}\right)^3\frac{J_3(|\mathbf{Q}_p|\,|\boldsymbol{\zeta}|)}{|\mathbf{Q}_p|^2-k^2}\right), \tag{14a}$$

and

$$S_0^{\mathrm{K,A}}(k,\boldsymbol{\kappa}) = \frac{1}{I_3(k|\boldsymbol{\zeta}|)}\left(K_3(k|\boldsymbol{\zeta}|) - \frac{8}{(k|\boldsymbol{\zeta}|)^3} + \frac{1}{k|\boldsymbol{\zeta}|} - \frac{k|\boldsymbol{\zeta}|}{8} + \frac{2\pi}{A}\sum_p\left(\frac{k}{|\mathbf{Q}_p|}\right)^3\frac{J_3(|\mathbf{Q}_p|\,|\boldsymbol{\zeta}|)}{|\mathbf{Q}_p|^2+k^2}\right), \tag{14b}$$

where $A = d\eta$, $\mathbf{Q}_p = \boldsymbol{\kappa} + \mathbf{K}_p$, and the vector $\boldsymbol{\zeta}$ represents an arbitrary vector positioned inside the first Brillouin zone with the condition $|\boldsymbol{\zeta}| < 1$. Here, we have used an acceleration parameter of 3, which is within the recommended range specified in [2]. We also define the following reciprocal array vector

$$\mathbf{K}_p = \frac{2\pi}{d\eta}(m\eta, nd - m\xi), \quad \text{for } p = (m,n) \in \mathbb{Z}_2, \tag{15}$$

which corresponds to the real space array vector (3).

Note that the array sum $S_0^{\mathrm{Y,A}}(k,\boldsymbol{\kappa})$ which features in our dispersion relation (13) is singular for $|\mathbf{Q}_p| = k$. This relation allows us to determine the singularity surfaces of the plate over the entire Brillouin zone and determine the band surfaces straightforwardly.[4]

In order to both closely understand plane wave propagation through the crystal and to verify the band surfaces for our doubly periodic array, we will also construct the solution to a large finite stack of hexagonally arranged gratings and examine the reflectance and transmission. We proceed by constructing the reflection and transmission matrices associated with a single grating.

4. Wave scattering by a single grating of pinned points

In this section, we investigate the reflection and transmission spectrum for a single grating of pins. The solution to this problem using multipole techniques is well-known and is outlined in [6]. We provide a brief summary of the results here and begin by populating the reflection and transmission matrices for a single grating. These matrices are constructed by considering incident plane waves of the form

$$w_{\mathrm{I}}^{\mathrm{H}} = \frac{\delta_0}{\sqrt{|\chi_0|}} \mathrm{e}^{\mathrm{i}\mathbf{k}_0\cdot\mathbf{x}}, \qquad \text{and} \qquad w_{\mathrm{I}}^{\mathrm{M}} = \frac{\widehat{\delta}_0}{\sqrt{|\widehat{\chi}_0|}} \mathrm{e}^{\mathrm{i}\mathbf{k}_0\cdot\mathbf{x}}, \tag{16}$$

which correspond to waves travelling in the direction $y < 0$ (i.e. from above) at normalized amplitudes δ_0 and $\widehat{\delta}_0$, at angles θ_i, and at a specified wave number k. We write these incident waves compactly in terms of the incident wave vector $\mathbf{k}_0 = (\alpha_0, -\chi_0) = (k\sin\theta_i, -k\cos\theta_i)$. Such waves will be scattered by the pinned grating and give rise to channels α_n which are given by the Fraunhofer grating equation:

$$\alpha_n = k\sin(\theta_n) = \alpha_0 + \frac{2\pi n}{d}, \tag{17}$$

[28] with the vertical wave vector components

$$\chi_n = \begin{cases} \sqrt{k^2 - \alpha_n^2}, & \alpha_n^2 \le k^2 \\ \mathrm{i}\sqrt{\alpha_n^2 - k^2}, & \alpha_n^2 > k^2 \end{cases}, \qquad \widehat{\chi}_n = \mathrm{i}\sqrt{k^2 + \alpha_n^2}. \tag{18}$$

Using these parameters, the reflection and transmission coefficients for an array of pins can be obtained analytically [4] and are given by

$$R_m^{\mathrm{H}} = \frac{2\sqrt{|\chi_m|}}{\chi_m d} E_0^{\mathrm{H}}, \quad T_m^{\mathrm{H}} = R_m^{\mathrm{H}} + \delta_{m0}, \quad R_m^{\mathrm{M}} = T_m^{\mathrm{M}} = \frac{2\sqrt{|\chi_m|}}{\chi_m d} E_0^{\mathrm{M}}, \tag{19a}$$

$$\widehat{R}_m^{\mathrm{M}} = \frac{2\mathrm{i}}{d\sqrt{|\widehat{\chi}_m|}} E_0^{\mathrm{M}}, \quad T_m^{\mathrm{M}} = \widehat{R}_m^{\mathrm{M}} + \delta_{m0}, \quad \widehat{R}_m^{\mathrm{H}} = \widehat{T}_m^{\mathrm{H}} = \frac{2\mathrm{i}}{d\sqrt{|\widehat{\chi}_m|}} E_0^{\mathrm{H}} \tag{19b}$$

where

$$E_0^{\mathrm{H}} = \frac{1}{\sqrt{|\chi_0|}} E_0, \quad E_0^{\mathrm{M}} = \frac{1}{\sqrt{|\widehat{\chi}_0|}} E_0, \tag{20a}$$

$$E_0 = -\frac{d}{2}\left[\sum_{p\in\Omega_{\mathrm{H}}}\left(\frac{1}{\chi_p} - \frac{1}{\widehat{\chi}_p}\right) + \mathrm{i}\sum_{p\in\bar{\Omega}_{\mathrm{H}}}\left(\frac{1}{|\widehat{\chi}_p|} - \frac{1}{|\chi_p|}\right)\right]^{-1}, \tag{20b}$$

and we have the sets $\Omega_{\mathrm{H}} = \{p : \chi_p \in \mathbb{R}\}$ and $\bar{\Omega}_{\mathrm{H}} \in \mathbb{Z}\backslash\{\Omega_{\mathrm{H}}\}$. Using these reflection and transmission expressions, we are then able to construct the relevant matrices for a single grating

$$\mathbf{R}_1^{(0)} = \left[\begin{array}{c|c} \mathbf{R}_{\mathrm{HH}}^{(0)} & \mathbf{R}_{\mathrm{HM}}^{(0)} \\ \hline \mathbf{R}_{\mathrm{MH}}^{(0)} & \mathbf{R}_{\mathrm{MM}}^{(0)} \end{array}\right], \quad \text{and} \quad \mathbf{T}_1^{(0)} = \left[\begin{array}{c|c} \mathbf{T}_{\mathrm{HH}}^{(0)} & \mathbf{T}_{\mathrm{HM}}^{(0)} \\ \hline \mathbf{T}_{\mathrm{MH}}^{(0)} & \mathbf{T}_{\mathrm{MM}}^{(0)} \end{array}\right], \tag{21}$$

where the (p,q)th element of $\mathbf{R}_{\mathrm{HH}}^{(0)}$ is R_p^{H} which corresponds to a Helmholtz incident wave $w_{\mathrm{I}}^{\mathrm{H}}$ travelling down the channel $\alpha_q = \alpha_0 + 2\pi q/d$. Similarly, the (p,q)th element of $\mathbf{R}_{\mathrm{MH}}^{(0)}$ is $\widehat{R}_p^{\mathrm{H}}$ corresponding to $w_{\mathrm{I}}^{\mathrm{H}}$ down the channel α_q. Finally, the (p,q)th elements of

$\mathbf{R}^{(0)}_{\mathrm{HM}}$ and $\mathbf{R}^{(0)}_{\mathrm{MM}}$ are R^{M}_p and $\widehat{R}^{\mathrm{M}}_p$, respectively, corresponding to w^{M}_1 down channel α_q. The transmission matrix $\mathbf{T}^{(0)}_1$ is created in an analogous manner to the definitions above.[6,10]

Due to the symmetry of the scatterer (a zero-radius circular cylinder), the reflection and transmission matrices corresponding to plane incident wave scattering from below are identical to those corresponding to incidence from above, i.e. $\mathbf{R}'^{(0)}_1 = \mathbf{R}^{(0)}_1$ and $\mathbf{T}'^{(0)}_1 = \mathbf{T}^{(0)}_1$. We now proceed to derive the matrices for N grating stacks arranged as a finite hexagonal array (as seen in Figure 2).

5. Wave scattering by finite stacks of pinned gratings

In this section, we consider the problem of multiple grating stacks. We will outline the recurrence relation procedure for determining the reflection and transmission matrices associated with N grating layers based on the work of [6,29,30].

We begin by introducing the phase shifted matrices $\mathbf{R}_1, \mathbf{T}_1, \mathbf{R}'_1$, and $\mathbf{T}'_1$ which have phase origins which sit halfway between neighboring grating layers, as opposed to the center of each grating. We define these matrices as

$$\begin{aligned} \mathbf{R}_1 &= \mathbf{Q}\mathbf{P}\mathbf{R}^{(0)}_1\mathbf{P}\mathbf{Q}^{-1}, \quad \mathbf{T}_1 = \mathbf{Q}^{-1}\mathbf{P}\mathbf{T}^{(0)}_1\mathbf{P}\mathbf{Q}^{-1}, \\ \mathbf{R}'_1 &= \mathbf{Q}^{-1}\mathbf{P}\mathbf{R}'^{(0)}_1\mathbf{P}\mathbf{Q}, \quad \mathbf{T}'_1 = \mathbf{Q}\mathbf{P}\mathbf{T}'^{(0)}_1\mathbf{P}\mathbf{Q}, \end{aligned} \tag{22}$$

where

$$\mathbf{P} = \left[\begin{array}{c|c} \mathbf{P}^{\mathrm{H}} & \mathbf{0} \\ \hline \mathbf{0} & \mathbf{P}^{\mathrm{M}} \end{array}\right], \quad \mathbf{P}^{\mathrm{H}}_{pq} = \delta_{pq}\mathrm{e}^{\mathrm{i}\chi_p\eta/2}, \quad \mathbf{P}^{\mathrm{M}}_{pq} = \delta_{pq}\mathrm{e}^{\mathrm{i}\widehat{\chi}_p\eta/2}, \tag{23a}$$

$$\mathbf{Q} = \left[\begin{array}{c|c} \mathbf{Q}^{\mathrm{H}} & \mathbf{0} \\ \hline \mathbf{0} & \mathbf{Q}^{\mathrm{M}} \end{array}\right], \quad \mathbf{Q}^{\mathrm{H}}_{pq} = \mathbf{Q}^{\mathrm{M}}_{pq} = \delta_{pq}\mathrm{e}^{\mathrm{i}\alpha_p\xi/2}. \tag{23b}$$

Using these shifted matrices, one can then use the recurrence relation associated with plane wave scattering from above:

$$\mathbf{R}_{n+1} = \mathbf{R}_1 + \mathbf{T}'_1\mathbf{R}_n\left(\mathbf{I} - \mathbf{R}'_1\mathbf{R}_n\right)^{-1}\mathbf{T}_1, \tag{24a}$$

$$\mathbf{T}_{n+1} = \mathbf{T}_n\left(\mathbf{I} - \mathbf{R}'_1\mathbf{R}_n\right)^{-1}\mathbf{T}_1, \tag{24b}$$

to determine $\mathbf{R}_N$ and $\mathbf{T}_N$ associated with N grating stacks.[4,30] Alternatively, one could use the transfer matrix approach outlined in [29]. However, we have found that this procedure is difficult for $N \geq 3$ as it involves the inversion of matrices with large condition numbers. It is then possible to determine the matrices $\mathbf{R}'_N$ and $\mathbf{T}'_N$ via the reciprocity relations given by equations (7.5) to (7.10) in [6].

After the recurrence relation procedure, one can then rephase our final $\mathbf{R}_N$ and $\mathbf{T}_N$ matrices, so that the phase origins sit at the center of the grating layer. This is done via

$$\mathbf{R}^{(0)}_N = \mathbf{P}^{-1}\mathbf{Q}^{-1}\mathbf{R}_N\mathbf{Q}\mathbf{P}^{-1}, \tag{25a}$$

$$\mathbf{T}^{(0)}_N = \mathbf{P}^{-1}\mathbf{Q}\mathbf{T}_N\mathbf{Q}\mathbf{P}^{-1}. \tag{25b}$$

The reflection and transmission amplitudes associated with N grating layers can then be obtained by multiplying the matrices $\mathbf{R}_N$ and $\mathbf{T}_N$ by $\boldsymbol{\delta}$ which is a vector containing the input amplitudes for wave incidence from above.

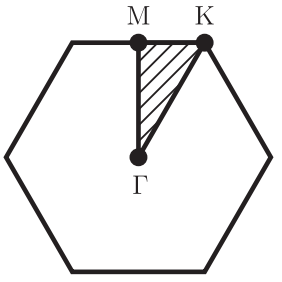

Figure 1. An outline of the Brillouin zone and irreducible Brillouin zone for a hexagonal array (shaded), with the symmetry points Γ at the origin, M at the center of a rectangular face and K at the middle of an edge joining two rectangular faces.

6. Conservation of energy relation

An additional check on numerics can be done using the energy balance relation in Equation (7.3) of [6] which was expressed in matrix form by [10] as

$$\mathbf{R}^{\mathrm{T}}\mathbf{U}\mathbf{R}^{*} + \mathbf{T}^{\mathrm{T}}\mathbf{U}\mathbf{T}^{*} = \mathbf{U} - \mathrm{i}\left(\mathbf{V}\mathbf{R}^{*} - \mathbf{R}^{\mathrm{T}}\mathbf{V}^{\mathrm{T}}\right), \tag{26}$$

where

$$\mathbf{U} = \left[\begin{array}{c|c} \mathbf{U}^{\mathrm{H}} & \mathbf{0} \\ \hline \mathbf{0} & \mathbf{0} \end{array}\right], \quad \mathbf{V} = \left[\begin{array}{c|c} \mathbf{V}^{\mathrm{H}} & \mathbf{0} \\ \hline \mathbf{0} & \mathbf{V}^{\mathrm{M}} \end{array}\right], \tag{27a}$$

$$\mathbf{U}^{\mathrm{H}}_{pq} = \beta_p \delta_{pq}, \quad \mathbf{V}^{\mathrm{H}}_{pq} = (\beta_p - 1)\delta_{pq}, \quad \mathbf{V}^{\mathrm{M}}_{pq} = \delta_{pq}, \quad \beta_n = \begin{cases} 1, & \alpha_n^2 \le k^2 \\ 0, & \alpha_n^2 > k^2, \end{cases} \tag{27b}$$

and star notation denotes complex conjugate operation. The expression (26) is valid for any reflection and transmission matrix pair corresponding to any number of grating stacks.

7. Results and discussion

We begin by investigating a hexagonal array of period $d = 1$, which has the array vectors:

$$\mathbf{R}_p = m\begin{pmatrix} 1 \\ 0 \end{pmatrix} + n\begin{pmatrix} 1/2 \\ \sqrt{3}/2 \end{pmatrix}, \tag{28a}$$

$$\mathbf{K}_p = \frac{4\pi}{\sqrt{3}}\left[m\begin{pmatrix} \sqrt{3}/2 \\ -1/2 \end{pmatrix} + n\begin{pmatrix} 0 \\ 1 \end{pmatrix}\right], \quad \text{for } p = (m, n) \in \mathbb{Z}_2. \tag{28b}$$

We also parametrize the edge of the Brillouin zone using the expressions:

$$\begin{aligned} \Gamma\mathrm{M} &: (\kappa_x, \kappa_y) = (0, t) && 0 \le t \le 2\pi/\sqrt{3}, \\ \mathrm{MK} &: (\kappa_x, \kappa_y) = \left(t, 2\pi/\sqrt{3}\right) && 0 \le t \le 2\pi/3, \\ \mathrm{K}\Gamma &: (\kappa_x, \kappa_y) = \left(t/2, \sqrt{3}t/2\right) && 0 \le t \le 4\pi/3, \end{aligned} \tag{29}$$

which follow from Figure 1 and are given in [29].

From this we obtain the band diagram in Figure 3 which has several interesting features. The first of these is a complete band gap in the interval $0 < k < 3.6276$ and the presence of partial gaps thereafter, particularly for $\kappa_x = 0$. This band diagram also features a double

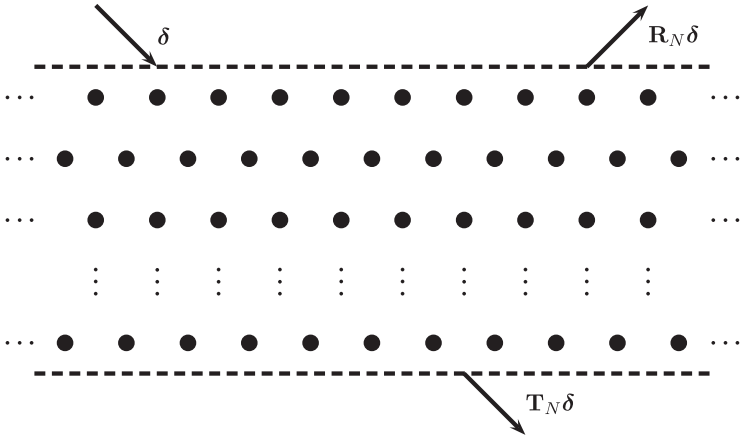

Figure 2. An outline of plane wave scattering (from above) through a stack of N hexagonally arranged pinned gratings.

Dirac cone at Γ for $k = 7.2552$, which is characterized by two band surfaces from above and two band surfaces from below collapsing as cones onto a central flat band surface (where the flatness of the band is in reference to the immediate vicinity of the origin).[16] The black dotted lines in Figure 3 correspond to light lines and here we see a typical but important feature of pinned band diagrams: the presence of bands sandwiched between light lines.[4] We observe that the trajectories of the band surfaces at the first Dirac point ($k = 7.2552$) approach along light lines in one direction (i.e. KΓ) and exit freely along the other parametrized direction (i.e. ΓM), forming an alternating pattern for increasing k. Note that these light lines are typically degenerate at symmetry points and therefore mode counting at these points is not obvious.

The isofrequency contours of the central flat band near the origin are given in Figure 3(b) where we can see that the contours exhibit sextic (hexagonal) degeneracy for $\boldsymbol{\kappa} \to \mathbf{0}$, in contrast to the circular contours for the other degenerate bands. The curvature along each segment of the hexagonal contours is minimal and hence the crystal would exhibit strong collimation.[31] In Figure 3(c), the isofrequency contours for the same band are given over the domain $(\kappa_x, \kappa_y) = [-2\pi, 2\pi] \times [-2\pi, 2\pi]$, along with an outline of the Brillouin zone given in white. Here, we can clearly see a minimum of $k = 7.2552$ at the origin, maximum values of $k = 8.3396$ at the edges of the Brillouin zone, and saddle points at $k = 7.7821$ which are located in the center of each face along the hexagonal Brillouin zone. This central band bears similarity to the structure of benzene, which is often drawn as six carbon atoms in a ring surrounded by six hydrogen atoms. We also see that long and flat isofrequency contours persist throughout most of the Brillouin zone, which would correspond to strongly collimated beam propagation inside the crystal.

A three-dimensional picture of these Dirac point band surfaces is given in Figure 4 in the immediate vicinity of the origin, where we can clearly see the band surfaces above and below collapsing as cones, with a central flat band whose isofrequency contours are given previously in Figure 3(b) over the same domain. This very flat band surface in the center of these collapsing bands is associated with slow light in photonics and slow vibration in platonics.[32] A careful examination of the band diagram over a wide k interval reveals Dirac points at the origin for $k = 7.2552$, $k = 12.5664$, and $k = 14.5104$ which each

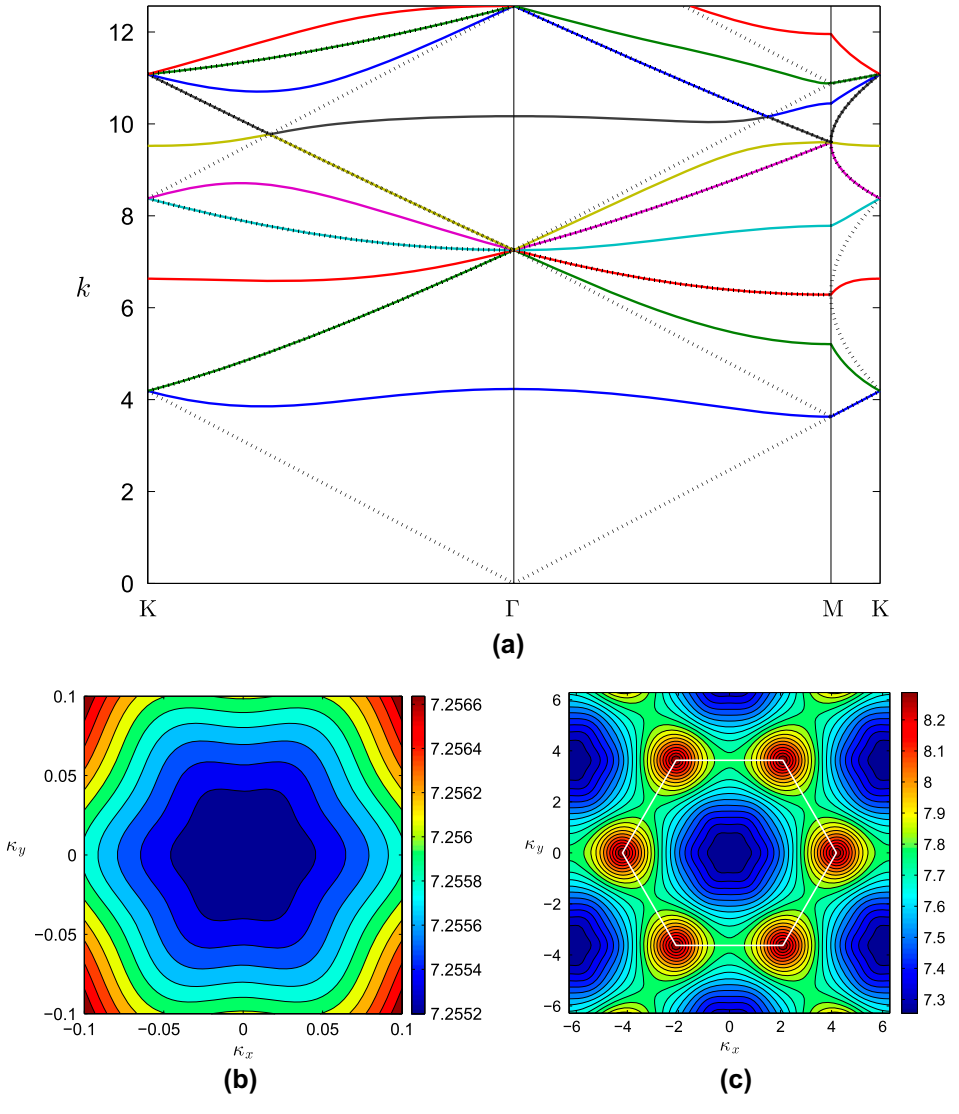

Figure 3. (Color online) The band diagram for (a) a hexagonally pinned plate ($d = 1$) which plots the wave number k as a function of $\boldsymbol{\kappa}$ as we trace a path through the Brillouin zone. Isofrequency contours for the central band (at $k = 7.2552$) are also given (b) near the origin and (c) over multiple Brillouin zones. An outline of the first Brillouin zone for a hexagonal lattice is shown.

feature identical degeneracy, with five degenerate bands present (i.e. two degenerate conical bands above and below with a central flat band). However, at $k = 19.1954$ we have 11 degenerate bands collapsing at Γ (i.e., five above and below, with a central flat band). Further, Dirac points involving a large number of degenerate bands can be found at higher frequencies, however we consider wave numbers up to the fifth Dirac point at $k = 21.7656$ for convenience.

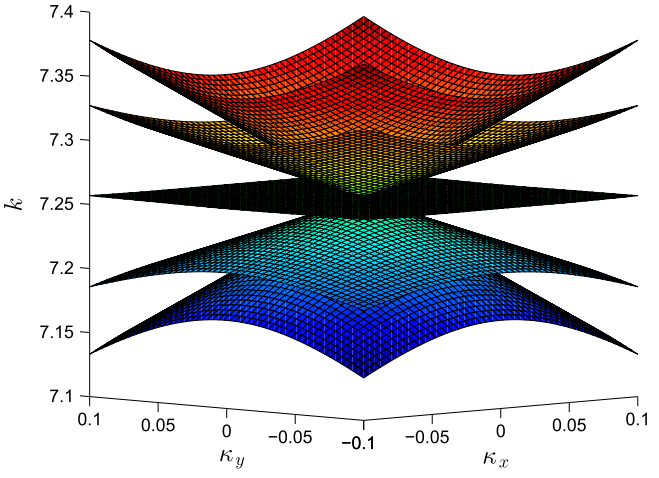

Figure 4. (Color online) A three-dimensional image of the band surfaces near Γ for the first Dirac point at $k = 7.2552$.

In Figure 5(a), we see a menagerie of mode behaviors including partial band gaps (particularly at Γ), flat bands, bands sandwiched between light lines, and a multitude of avoided crossings all centered about a double Dirac point at $k = 19.1954$ where 11 bands collapse at the origin. In Figure 5(b), the isofrequency contours for the central band about the origin are given where we see distorted hexagonal contours, that is, the line segments of a hexagonal polygon are quartic in nature. It is clear that collimation is not supported here, however the band is especially flat about the origin. This is confirmed in Figure 5(c) where the band surface is computed over the domain $(\kappa_x, \kappa_y) = [-2\pi, 2\pi] \times [-2\pi, 2\pi]$. In this figure, we have a similar benzene ring design to Figure 3(c) except that we have 12 absolute maxima spaced in a sunflower geometry at $k = 19.3384$, absolute maxima at $k = 18.2907$ at the edges of the Brillouin zone, relative minima ($k = 18.8509$) at the center of each hexagonal face which are flanked on the left and right by saddle points at $k = 18.9349$. At the origin, we have a relative maximum of $k = 19.1954$. This central flat band occupies the interval $18.2907 < k < 19.3384$, which is of comparable range to the central band for the first Dirac point (which occupies the interval $7.2552 < k < 8.3396$). Note that these central bands exhibit minimal curvature in the vicinity of the origin and comparatively less curvature over the entire Brillouin zone, relative to neighboring degenerate bands (see Figures 3 and 4 for reference). As mentioned previously, such flat bands are associated with near-zero group velocities, and subsequently slow vibration propagation through platonic crystals.[10,32] Similar effects can be observed in photonics where structures are often engineered to achieve slow light propagation.[33,34]

In Figure 6(a), the isofrequency contours at $k = 18.7000$ are given (below the Dirac point at $k = 19.1954$), which features six band surfaces (including the central flat band) and exhibit intricate curvatures. These degenerate band surfaces are of varied geometry and range from circles to hexagons and even shapes reminiscent of polar flowers, or rhodonea curves. In Figure 6(b), we consider the isofrequency curves in a smaller region about the origin, and observe two circular contours (dashed curves) and two hexagonal contours (solid curves), which persist in their shape as we approach the Dirac point (as $k \to 19.1954$).

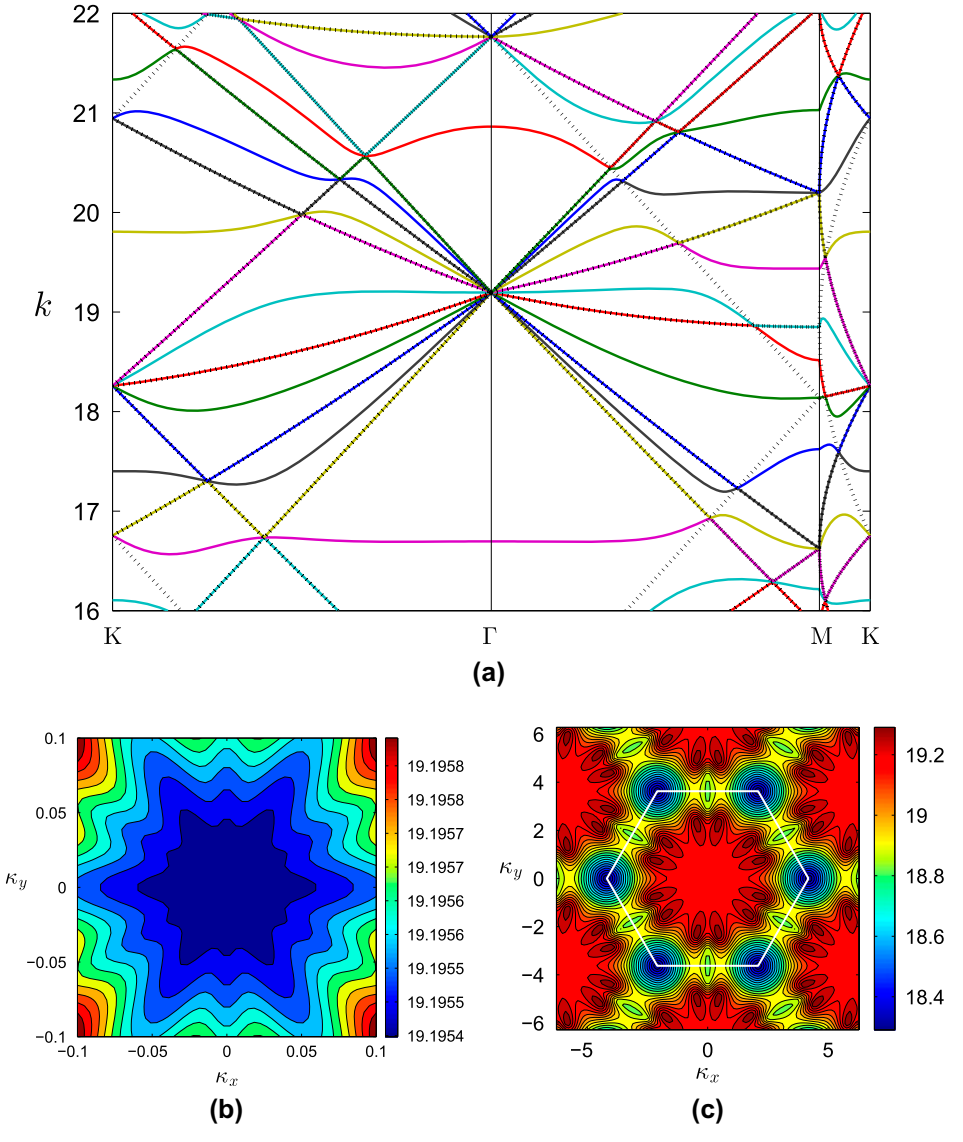

Figure 5. (Color online) The band diagram for (a) a hexagonally pinned plate ($d = 1$) at higher wave numbers, obtained by tracing a path through the Brillouin zone. The isofrequency contours for the central band (at $k = 19.1954$) are given (b) in the vicinity of the origin, and (c) over multiple Brillouin zones. An outline of the first Brillouin zone for a hexagonal lattice is shown.

Consequently, we have a double Dirac cone towards $k = 19.1954$ which is nested inside collapsing bands of non-circular geometry. Identical isofrequency curves can also be seen above the Dirac point considered here.

In Figure 7(a), we plot the total reflectance for a stack of 200 gratings which are arranged in the form of a hexagonal lattice. For this figure, the reflectance curve is drawn for a normally incident plane wave $w_{\mathrm{I}}^{\mathrm{H}}(\mathbf{x})$ (given in (16)). The intervals of 100% reflection seen

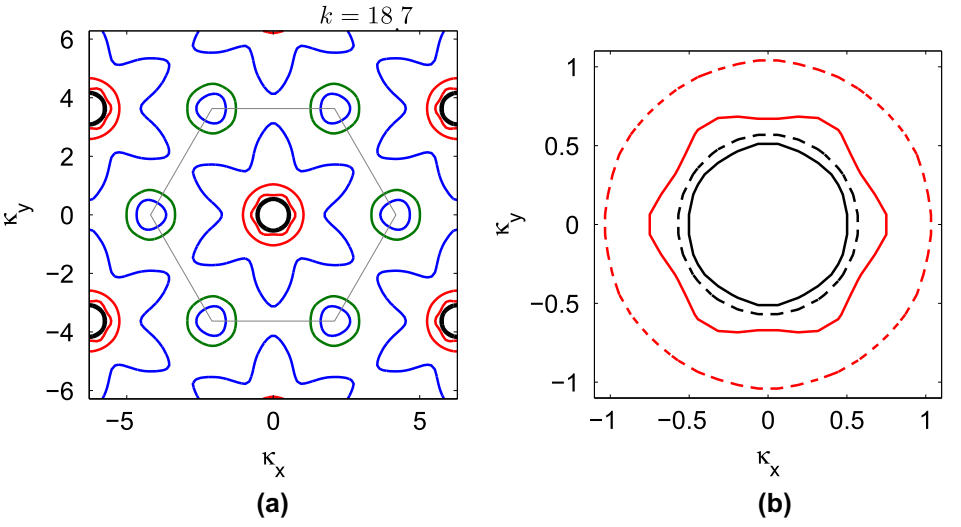

Figure 6. (Color online) Isofrequency contours at $k = 18.7000$ for a hexagonal lattice $d = 1$ below the Dirac point (at $k = 19.1952$) (a) over the entire Brillouin zone, and (b) in the region near the origin.

here coincide with the band gaps observed in the band diagrams (presented in Figure 3(a) and Figure 5(a)), which are computed separately using the dispersion relation (13). This gives us strong confidence in the validity of the results presented here. Note that for normal incidence, we have double Wood anomalies at $k = 2n\pi$ for $n = 0, 1, 2\ldots$ which each correspond physically to the birth of two surface waves which propagate along the top and bottom of the stack in both directions. These Wood anomalies may in certain circumstances have a wide influence on the computed spectra, and here for example, a double Wood anomaly coincides with a double Dirac point at Γ for $k = 12.5664$ giving rise to minimal reflectance of energy. Other interesting behavior can also be seen here, including oscillations in reflectance across the interval $7.2552 < k < 7.7838$ after the first Dirac point. A closer examination of this is made in Figure 7(b) where we consider the transmittance of the 200-layered stack in the interval $7 < k < 8$, where resonant spikes in transmission can be seen. These transmission spikes are densely packed and at first glance may appear to represent a random transmission phenomenon. However, this is not the case, as in Figures 8(a) and (b), we can clearly see that the number of transmission spikes is a function of the number of grating layers. In Figure 8(a), we have five hexagonally arranged grating stacks giving rise to four resonant spikes in transmission (all of varying Q-factors and amplitudes [9]), and in Figure 8(b), we have 10 layers giving nine resonances in transmission. Interestingly, as we increase the number of gratings, the peaks become dense at the edges of the interval $7.2552 < k < 7.7838$, which is an indication of slow wave propagation.[34] Accordingly, for N grating layers we have $N - 1$ spikes in transmission across this interval. These enhanced transmission spikes are caused by a constructive Fabry–Perot interference phenomenon, which arises from interactions between the flat band and other band surfaces.

This can be seen clearly in Figures 9(a)–(c), where we have computed the isofrequency contours for our hexagonal (doubly periodic) array at a prescribed wave number k, as well as the associated three-dimensional band surfaces (with a horizontal plane at fixed frequency added for reference). In Figure 9(a), we can see that for $k = 7.0328$ we have two circular

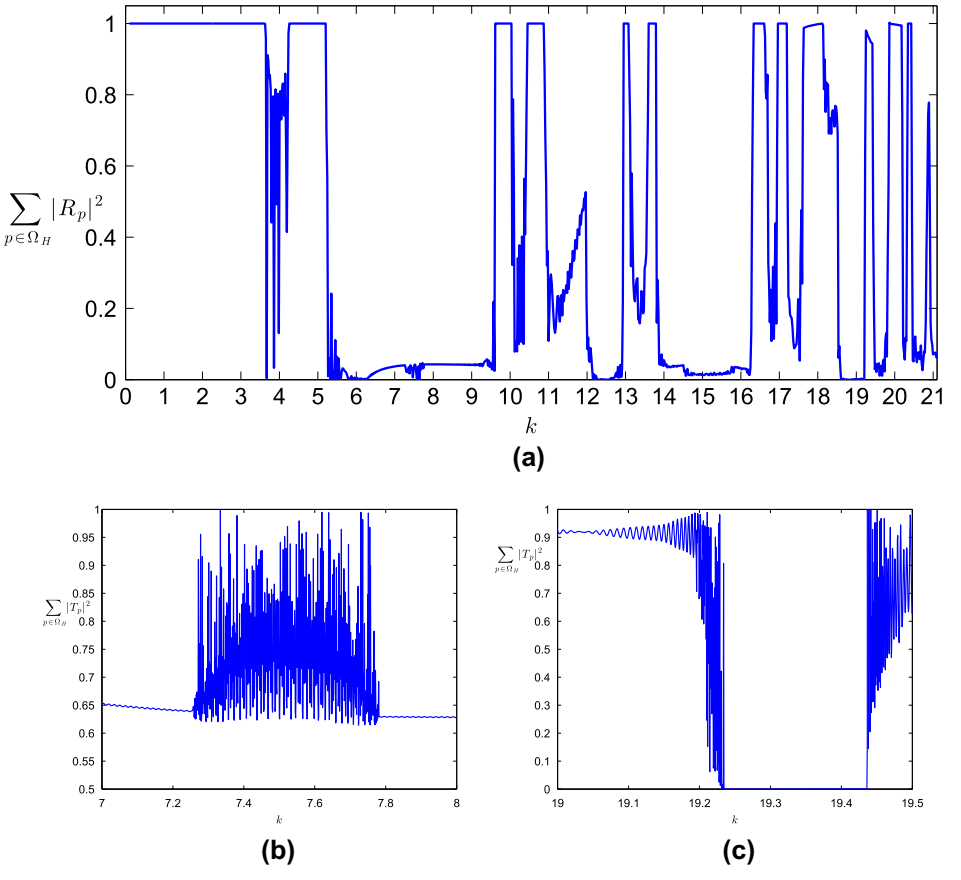

Figure 7. (Color online) (a) The reflectance of a stack of 200 hexagonally arranged pinned gratings, (b) the transmission spectrum in the immediate vicinity of the first Dirac point which features resonant spikes in transmission, and (c) the transmission near the Dirac point at $k = 19.1954$ which features both resonant transmission and an interval of near zero transmission.

contours which are small in radius, and are centered about the origin, corresponding to two degenerate conical bands. Although small in radius, these surfaces have a group velocity significant enough to support wave propagation through the associated platonic crystal, which can be seen in Figure 7(a). In Figure 9(b), we present the contour plot and band surfaces for a wave number inside the interval of resonant transmission ($k = 7.6181$). Here, the central flat band is given in red, with the two upper bands given in blue and green. As each of these contour curves correspond to different Bloch modes, we can see that for normal incidence there is significant competition for which mode transports energy. In other words, the presence of this central flat band gives rise to an interference phenomenon between the flat band and other band surfaces. In Figure 9(c), we consider the contours for $k = 7.7838$ where we see that the central band (in red) assumes an elegant flower petal geometry and possesses an emergent band gap at $\kappa_x = 0$, which coincides with the end of resonant transmission.

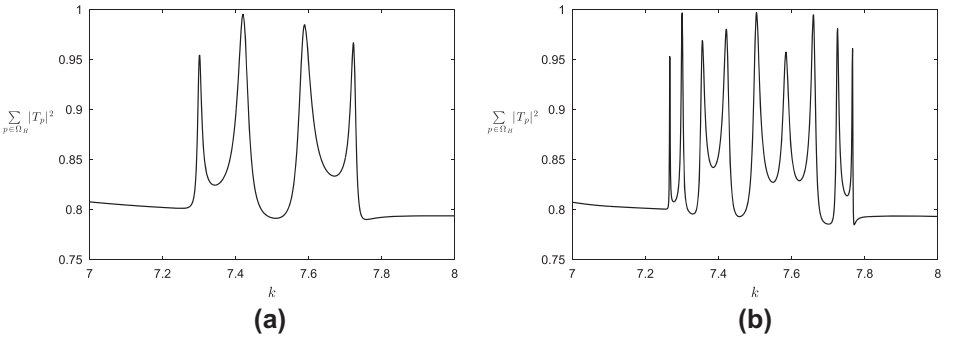

Figure 8. The transmittance of (a) 5 hexagonally stacked gratings and (b) the transmittance for 10 stacks.

Returning to Figure 7(c), we examine the transmittance of a hexagonally arranged stack of 200 gratings from $18 < k < 19.5$ (i.e. in the vicinity of the Dirac point at $k = 19.1954$). This transmission spectrum features resonant transmission, however it also possesses an interval of a near-zero transmission (where slow light propagates at low amplitudes). This emphasizes that the wave behavior from one Dirac point to the next can be very different, and that the dynamics of the crystal at high wave number depends strongly on the relative curvature of neighboring band surfaces. This is demonstrated in Figures 10(a)–(c), which plot the isofrequency contours and band surfaces in the vicinity of the Dirac point at $k = 19.1954$. In Figure 10(a), we see a snowflake contour in green, which corresponds to the central flat band. Here, there are also a host of degenerate band surfaces at the origin, however these are of small radius and not easily visible. Nevertheless, they still possess group velocities of sufficient magnitude to cause resonant transmission. In Figure 10(b), we see the contours for $k = 19.2539$ which feature a sunflower geometry of 12 petals corresponding to the central flat band (in green). In this contour image, we can clearly see an emergent band gap for the central flat band at $\kappa_x = 0$, however we also see contours near the origin which arise from another relatively flat band above the central Dirac point band. This transports wave energy at both low amplitudes and low group velocities, and so the transmission curve in Figure 7(c) does not correspond to a perfect band gap. In Figure 10(c), we consider the band surface contours at $k = 19.4457$ (which lies beyond the interval of minimal transmission), which all feature complex curvature, including a Star of David geometry. Here, there is an overlapping of flat bands with non-flat bands, reminiscent of Figure 9(c), which accounts for the resonant transmission which features in Figure 7(c) after the interval of minimal transmission.

The transmission amplitudes in Figures 8(a) and (b) are summarized in Table 1 for reference, and for convenience we use the parameter

$$T_{\text{tot}} = \sum_{p \in \Omega_{\text{H}}} |T_p|^2$$

to denote the total energy transmitted by the grating stack. Also included is a column of Q-factors (Quality factors), which range from $Q = 180$ to $Q = 525$ for $N = 5$ layers and $Q = 500$ to $Q = 4037$ for $N = 10$ layers. In general, a Q-factor is a measure of resonance strength, and can be obtained by dividing the resonant wave number by the beam broadness

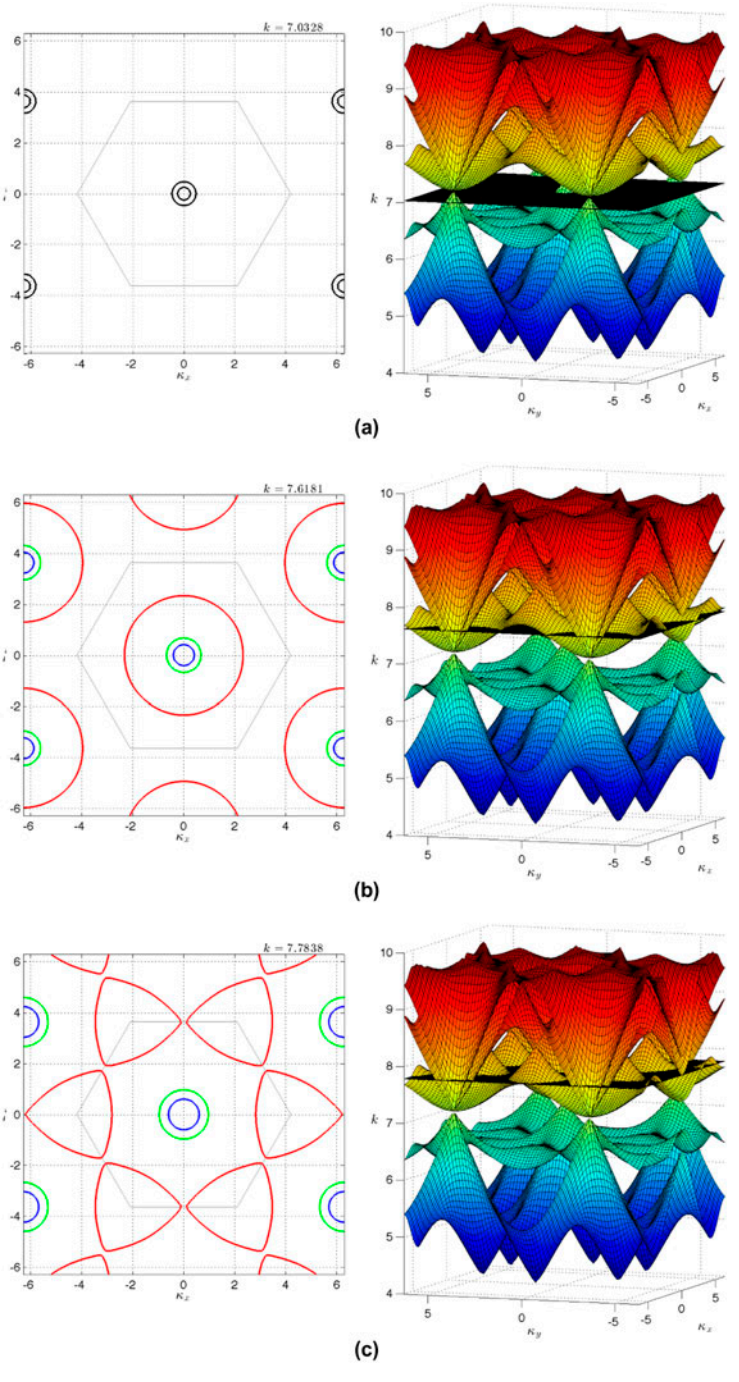

Figure 9. (Color online) Band surfaces and isofrequency contours for a hexagonal lattice $d = 1$ in the vicinity of the first Dirac point (at $k = 7.2552$) (a) below the Dirac point, (b) above the Dirac point (in the region of transmission spikes), and (c) at the saddle point of the flat central band.

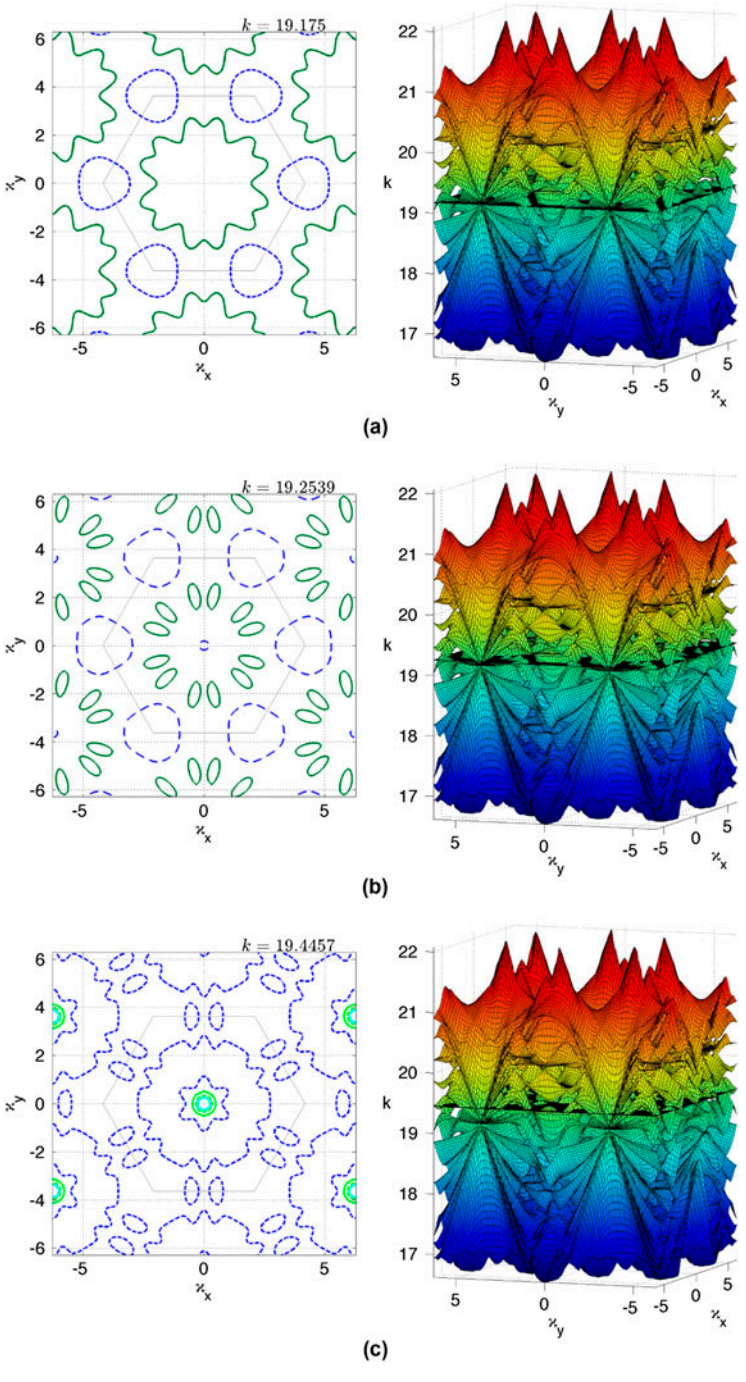

Figure 10. (Color online) Band surfaces and isofrequency contours for a hexagonal lattice $d = 1$ in the vicinity of the Dirac point at $k = 19.1952$ (a) below the Dirac point, (b) above the Dirac point but inside the band gap and (c) after the band gap where we see resonant spikes in transmission.

Table 1. Resonant frequencies k for a hexagonally arranged stack of pinned gratings, with total transmission amplitudes, T_{tot}, and Q-factors for finite stacks of depth $N = 5$ and $N = 10$.

N	Resonant frequency	T_{tot} value	Q-factor
5	$k = 7.3015$	0.9549	525
	$k = 7.4207$	0.9951	245
	$k = 7.5892$	0.9846	181
	$k = 7.7230$	0.9665	511
10	$k = 7.2669$	0.9533	4037
	$k = 7.3007$	0.9985	1178
	$k = 7.3563$	0.9691	500
	$k = 7.4216$	0.9805	505
	$k = 7.5042$	0.9969	363
	$k = 7.5847$	0.9573	429
	$k = 7.6597$	0.9949	594
	$k = 7.7257$	0.9817	878
	$k = 7.7667$	0.9751	3236

at half-amplitude.[9] As we increase the number of layers N, the average Q-value of each peak becomes increasingly large, as there are a dense number of resonances in the interval $7.2552 < k < 7.7838$ at high N.

8. Conclusions

In summary, we have demonstrated the existence of Dirac cone dispersion at the center of the Brillouin zone for pinned platonic crystals. This work is the first investigation on doubly periodic hexagonal lattices in platonics and is the first to demonstrate the existence of double Dirac cones in platonic crystals. We have demonstrated that the Dirac points of this hexagonal lattice can involve several degenerate band surfaces, with double Dirac cones nested inside the contours. We have also shown the existence of resonant transmission through finite stacks of hexagonally arranged gratings, where the number of resonant peaks has been shown to be a function of the stack depth. This was obtained using an established recurrence relation procedure, which was used to verify the accuracy of the band surfaces which were computed using accelerated array sums. Several band surface pictures and band diagrams are also presented which exhibit several interesting behaviors from wide band gaps to avoided crossings, and are used effectively to explain the resonant transmission phenomenon. Future work includes an investigation of hexagonal lattices which possess circular inclusions of finite radius, or even arbitrary geometries, subject to different boundary conditions at the edge. Alternatively, one could tune the periodicity of the lattice to see whether the Q-factors from transmission spikes could be improved, following from existing work by [8].

Additionally, future work in platonic crystals could be used in the design of future graphene structures, photonic crystals, phononic crystals, and other metamaterial structures. Possible applications of the interesting and complicated band properties described here could

arise in novel filtering applications involving either spatial or spectral selection. There would be interesting possibilities for the application of non-linear wave conversion at the Dirac points, although the complexity of such non-linear effects may well prove to be daunting.

Acknowledgements

R.C.M. would like to acknowledge the support of a Marie Curie Intra-European Fellowship and the Australian Research Council through its Discovery Grant Scheme. The Centre for Ultrahigh bandwidth Devices for Optical Systems (CUDOS) is an ARC Centre of Excellence (Project No. CE110001018).

References

[1] Smith MJA, McPhedran RC, Poulton CG, Meylan MH. Negative refraction and dispersion phenomena in platonic clusters. Wave Random Complex. 2012;22:435–458.
[2] Movchan AB, Movchan NV, McPhedran RC. Bloch-Floquet bending waves in perforated thin plates. Proc. R. Soc. A: Math. Phys. Eng. Sci. 2007;463:2505.
[3] Smith MJA, Porter R, Williams TD. The effect on bending waves by defects in pinned elastic plates. J. Sound Vib. 2012;331:5087–5106.
[4] McPhedran RC, Movchan AB, Movchan NV. Platonic crystals: Bloch bands, neutrality and defects. Mech. Mater. 2009;41:356–363.
[5] Meylan MH, McPhedran RC. Fast and slow interaction of elastic waves with platonic clusters. Proc. R. Soc. A: Math. Phys. Eng. Sci. 2011;467:3509–3529.
[6] Movchan NV, McPhedran RC, Movchan AB, Poulton CG. Wave scattering by platonic grating stacks. Proc. R. Soc. A: Math. Phys. Eng. Sci. 2009;465:3383.
[7] Haslinger SG, McPhedran RC, Movchan NV, Movchan AB. Localisation near defects and filtering of flexural waves in structured plates. Int. J. Fracture. 2013;1–17.
[8] Haslinger SG, Movchan NV, Movchan AB, McPhedran RC. Wave localisation in structured elastic plates. In: Náprstek J, Horáček J, Okrouhlík M, Marvalová B, Verhulst F, and Sawicki JT, editors. Vibration Problems ICOVP 2011. Dordrecht: Springer; 2011. p. 737–743.
[9] Haslinger SG, Movchan NV, Movchan AB, McPhedran RC. Transmission, trapping and filtering of waves in periodically constrained elastic plates. Proc. R. Soc. London. Series A: Math. Phys. Sci. 2012;468:76–93.
[10] Smith MJA, Meylan MH, McPhedran RC. Flexural wave filtering and platonic polarizers in thin elastic plates. Quarterly J. Mech. Appl. Math. 2013;66:437–463.
[11] Poulton CG, Movchan AB, Movchan NV, McPhedran RC. Analytic theory of defects in periodically structured elastic plates. Proc. R. Soc. A: Math. Phys. Eng. Sci. 2012;468:1196–1216.
[12] Geim, AK, Novoselov KS. The rise of graphene. Nat. Mater. 2007;6:183–191.
[13] Peleg O, Bartal G, Freedman B, Manela O, Segev M, Christodoulides DN. Conical diffraction and gap solitons in honeycomb photonic lattices. Phys. Rev. Lett. 2007;98:103901.
[14] Diem M, Koschny T, Soukoulis C. Transmission in the vicinity of the Dirac point in hexagonal photonic crystals. Phys. B: Condens. Matter. 2010;405:2990–2995.
[15] Sakoda K. Double Dirac cones in triangular-lattice metamaterials. Opt. Express. 2012;20:9925–9939.
[16] Liu R, Lai Y, Huang X, Chan CT. Dirac cones at $\vec{k} = 0$ in phononic crystals. Phys. Rev. B. 2011;84:224113.
[17] Li Y, Wu Y, Chen X, Mei J. Selection rule for Dirac-like points in two-dimensional dielectric photonic crystals. Opt. express. 2013;21:7699–7711.
[18] Huang X, Lai Y, Hang ZH, Zheng H, Chan C. Dirac cones induced by accidental degeneracy in photonic crystals and zero-refractive-index materials. Nat. Mater. 2011;10:582–586.

[19] Wang Z, Chong Y, Joannopoulos JD, Soljačić M. Reflection-free one-way edge modes in a gyromagnetic photonic crystal. Phys. Rev. Lett. 2008;100:013905.
[20] Antonakakis T, Craster R, Guenneau S. Moulding flexural waves in elastic plates lying atop a Faqir's bed of nails. arXiv, preprint arXiv:1301.7653.
[21] Torrent D, Mayou D, Sánchez-Dehesa J. Elastic analog of graphene: Dirac cones and edge states for flexural waves in thin plates. Phys. Rev. B. 2013;87:115143.
[22] Sepkhanov RA, Bazaliy YB, Beenakker CWJ. Extremal transmission at the Dirac point of a photonic band structure. Phys. Rev. A. 2007;75:063813.
[23] Poulton CG, McPhedran RC, Nicorovici NA, Botten LC. Localized GreenâĂŹs functions for a two-dimensional periodic material. In: Movchan AB, editor. IUTAM Symposium on Asymptotics, Singularities and Homogenisation in Problems of Mechanics. Boston (MA): Springer; 2004. p. 181–190.
[24] Movchan AB, Movchan NV, Poulton CG. Asymptotic models of fields in dilute and densely packed composites. London: Imperial College Press; 2002.
[25] Abramowitz M, Stegun IA. Handbook of mathematical functions with formulas, graphs, and mathematical tables. New York: Dover publications; 1972.
[26] Chin SK, Nicorovici NA, McPhedran RC. Green's function and lattice sums for electromagnetic scattering by a square array of cylinders. Phys. Rev. E. 1994;49:4590–4602.
[27] McPhedran RC, Nicorovici NA, Botten LC, Grubits KA. Lattice sums for gratings and arrays. J. Math. Phys. 2000;41:7808–7816.
[28] Born M, Wolf E. Principles of optics: electromagnetic theory of propagation, interference and diffraction of light. New York: Pergamon Press; 1964.
[29] Botten LC, Nicorovici NA, McPhedran RC, de Sterke M, Asatryan AA. Photonic band structure calculations using scattering matrices. Phys. Rev. E. 2001;64:046603.
[30] Platts SB, Movchan NV, McPhedran RC, Movchan AB. Two-dimensional phononic crystals and scattering of elastic waves by an array of voids. Proc. R. Soc. London. Series A: Math. Phys. Eng. Sci. 2002;458:2327–2347.
[31] Kosaka H, Kawashima T, Tomita A, Notomi M, Tamamura T, Sato T, Kawakami S. Self-collimating phenomena in photonic crystals. Appl. Phys. Lett. 1999;74:1212–1214.
[32] Poulton CG, McPhedran RC, Movchan NV, Movchan AB. Convergence properties and flat bands in platonic crystal band structures using the multipole formulation. Wave Random Complex. 2010;20:702–716.
[33] Baba T. Slow light in photonic crystals. Nat. Photonics. 2008;2:465–473.
[34] Spasenović M, White TP, Ha S, Sukhorukov AA, Kampfrath T, Kivshar YS, de Sterke CM, Krauss TF, Kuipers L. Experimental observation of evanescent modes at the interface to slow-light photonic crystal waveguides. Opt. Lett. 2011;36:1170–1172.